Advanced process-synchronized computed tomography for the investigation of periodic processes

Bieberle, A.; Neumann, M.; Hampel, U.;

Originally published:

July 2018

Review of Scientific Instruments 89(2018), 073111

DOI: https://doi.org/10.1063/1.5038423

Advanced process-synchronized computed tomography for the investigation of periodic processes

André Bieberle[1], Martin Neumann[1,2], Uwe Hampel[1,2]

[1] Institute of Fluid Dynamics, Helmholtz-Zentrum Dresden - Rossendorf, Bautzner Landstr. 400, 01328 Dresden, Germany.

[2] AREVA Endowed Chair of Imaging Techniques in Energy and Process Engineering, Technische Universität Dresden, 01062 Dresden, Germany.

Email: a.bieberle@hzdr.de

Abstract

Computed tomography (CT) is known for giving cross-sectional images of a body. As tomographic scans require mechanical movement of components, data acquisition is commonly too slow to capture dynamic processes, which are faster than the acquisition time for a single image. Time-averaged angle-resolved CT imaging is a more recent method, which has demonstrated a capability to sharply image fast rotating machinery components by synchronizing data acquisition with rotation. However, in this modality all information on static parts disappear. In this paper, a novel data acquisition approach is introduced that combines both CT imaging methods. Eventually, the developed method is exemplarily applied to the study of gas-liquid flow in an industrial centrifugal pump using high-resolution gamma-ray tomography imaging.

Key words

Tomographic imaging, synchronized data acquisition, multiphase flow, centrifugal pump

1 Introduction

Radiation based computed tomography (CT) is widely used for non-destructive testing, non-intrusive process analyses as well as for medical diagnostics. For conventional tomographic imaging, radiographic projections are acquired from different angular positions of the object of investigation by either rotating a source-detector assembly around the fixed object or by rotating the object in between the source and detector. Subsequently, the recorded attenuation projections are reconstructed to a cross-sectional image using e.g. filtered back projection or algebraic reconstruction techniques. The resulting images give the non-superimposed attenuation coefficient map of the object slice or volume [1]-[3].

Conventional radiographic computed tomography (*conv*CT) was originally developed for medical diagnostics with X-rays. Here, the patient is placed between a mechanically rotating source-detector assembly that continuously acquires slice images with high spatial resolution [4]-[6]. By synchronizing the progressive feed of the patient through the CT scanner, so-called helical CT imaging is performed providing complete volume scans of the body [7]. Furthermore, such full body CT scans are meanwhile synchronized with the electrocardiogram signals from the heart's systolic and diastolic phases in order to avoid motion artefacts [8]-[10]. Such synchronized CT imaging is also referred to as process-synchronized computed tomography (*ps*CT).

Meanwhile, computed tomography is an emerging technique for many industrial applications, too. Non-destructive testing is often applied for quality control of technical components and materials for example to detect inclusions, contact faults, fissures and cracks in integrated circuits, engines for aerospace applications but also for positioning and inspection of human implants [11]-[13]. Here, mainly X-ray tomography scanners have been developed and commercialized, providing images at high spatial resolution of static objects. In contrast, process tomography for troubleshooting, optimization and predictive maintenance in process equipment, such as chemical reactors, pumps or heat exchangers relies mainly on gamma radiation [14]-[19]. Harsh process environments, process dynamics, occurrence of multiphase flow as well as rotating equipment pose additional challenges for reliable CT imaging with respect to dynamic imaging. So far, process tomography has been applied mainly in a conventional manner providing time-averaged slice images of the material or fluid phase distributions, e.g. in various chemical reactors [20]-[27]. However, information about the process dynamics is often lost.

As a first step towards process-synchronized imaging, Prasser et al. (2003) introduced a novel CT imaging method called time-averaged angle-resolved CT (*tar*CT). They demonstrated the visualization of periodically changing gas fraction fields in an axial pump by synchronizing the data acquisition with the rotating parts of the pump and using an in-house developed radiation detector arc whose sampling frequency was significantly higher than the rotation frequency of the pump impeller [28]. With this approach, multiphase flows within various rotating equipment, e.g. stirred tanks [29], axial pumps [28], centrifugal pumps [32]-[34] and couplings [30]-[31], were further successfully studied. It should be mentioned that such synchronized CT data acquisition and imaging is not limited to rotating parts but can also be triggered by any kind of regular process intermittency such as periodic pulsation or flashing conditions as present for Taylor flow in capillaries [35] or for fuel injection in plunger pumps [36].

Hitherto, either *conv*CT or *tar*CT have been applied exclusively for multiphase flow investigations in rotating systems. Applying both CT imaging methods simultaneously would a) reduce the CT imaging time, b) improve the reliability and interpretability of static and dynamic results if the steady state of the process cannot be guaranteed and c) provide unique data on the dynamics of multiphase flows in process equipment with periodic behavior. The latter means, static as well as periodic parts can be reconstructed sharply. Eventually, images can be compiled as a sequence, which then shows the dynamics of a process along a period of the intermittency.

In the following, a novel approach for the simultaneous imaging with *conv*CT and *tar*CT is introduced, which we refer to as advanced process-synchronized CT (*adv*CT). The new method has been exemplarily applied to an industrial centrifugal pump operated in single-phase and two-phase flow conditions. As CT imaging system the high-resolution gamma-ray CT scanner [14], [29] was accordingly modified and applied.

2 Materials and Methods

2.1 CT imaging techniques

In general, computed tomography can be performed with either photon integrating detectors, delivering an analogue electrical voltage signal whose amplitude is proportional to the radiation photon flux, or photon counting detectors, delivering a digital number of radiation photons that are

counted within a projection interval. Since the CT system used in this study operates in photon counting mode, *adv*CT imaging is described in the following using the count rate notation.

Computed tomography bases on the acquisition of radiographic projections of an object from different angular positions. For each projection $i \in \mathbb{N} \mid 0 \leq i < N_\varphi$ the radiation intensity profile for all detector elements $d \in \mathbb{N} \mid 0 \leq d < N_d$ is stored in terms of counted radiation photons in a data matrix $S_{d,i}$. Thus, the count rates

$$\dot{S}_{d,i} = S_{d,i}/\Delta t_i \tag{1}$$

with the sampling interval Δt_i of each projection i. A reference CT scan $\dot{S}_{d,i}^{\mathrm{ref}}$ without object or with the object in a reference state is used to calculate the radiation attenuation data matrix (sinogram)

$$E_{d,i} = -\ln\left(\frac{\dot{S}_{d,i}}{\dot{S}_{d,i}^{\mathrm{ref}}}\right). \tag{2}$$

These data are then used to reconstruct the non-superimposed slice image of the averaged attenuation coefficients.

For *convCT imaging* the source-detector assembly (or respectively the object) is rotated with a slow rotation frequency f^{CT} and provides N_φ radiographic projections during a full $0° \leq \varphi < 360°$ rotation. Accordingly, the corresponding detector sampling frequency f^{samp} is defined by

$$f^{\mathrm{samp}} = N_\varphi \cdot f^{\mathrm{CT}}. \tag{3}$$

This way, a data matrix $\dot{S}_{d,i}^{\mathrm{conv}}$ of dimension $N_d \times N_\varphi$ is obtained wherein stationary parts of the object appear as sinusoidal structures. Thus, applying any CT reconstruction algorithm to the resulting $E_{d,i}^{\mathrm{conv}}$, static parts such as housings, baffles and nozzles are sharply reconstructed while moving parts, like rotating impellers, are smeared across the imaging plane (see Figure 1a).

For *tarCT imaging*, the source-detector assembly is not rotated, i.e. $f^{\mathrm{CT}} = 0$. Instead, the projection data acquisition is synchronized with periodically moving (rotating) parts of the object. In case of an impeller rotating with a given frequency f^{rot}, projection data are continuously sampled at a high frequency f^{samp}. Accordingly, the number of projections is given by

$$N_\alpha = f^{\mathrm{samp}}/f^{\mathrm{rot}}, \tag{4}$$

whereas f^{samp} must be significantly larger than f^{rot}. Typically, the statistics of detected photons within a single projection, i.e. the number of incident radiation photons in each single detector

element, is too low. Hence, all values of each detector element of each projection angle are added over a sufficient number of cycles, e.g. impeller revolutions. Synchronization can be performed by recording the signal of any suitable revolution sensor simultaneously with the projection data. In case of a rotating impeller, a Hall effect sensor might provide a zero-crossing signal for each revolution that corresponds to an acquisition interval $\Delta t_{zc} = 1/f^{\mathrm{rot}}$. Then, each detector reading (projection with index $j \in \mathbb{N} \mid 0 \leq j < N_\alpha$) corresponds to one angular position $\alpha_j = 2\,\pi j/N_\alpha$ of the impeller. Hence, the dimension of the data matrix $\dot{S}^{\mathrm{tar}}_{d,j}$ is $N_d \times N_\alpha$.

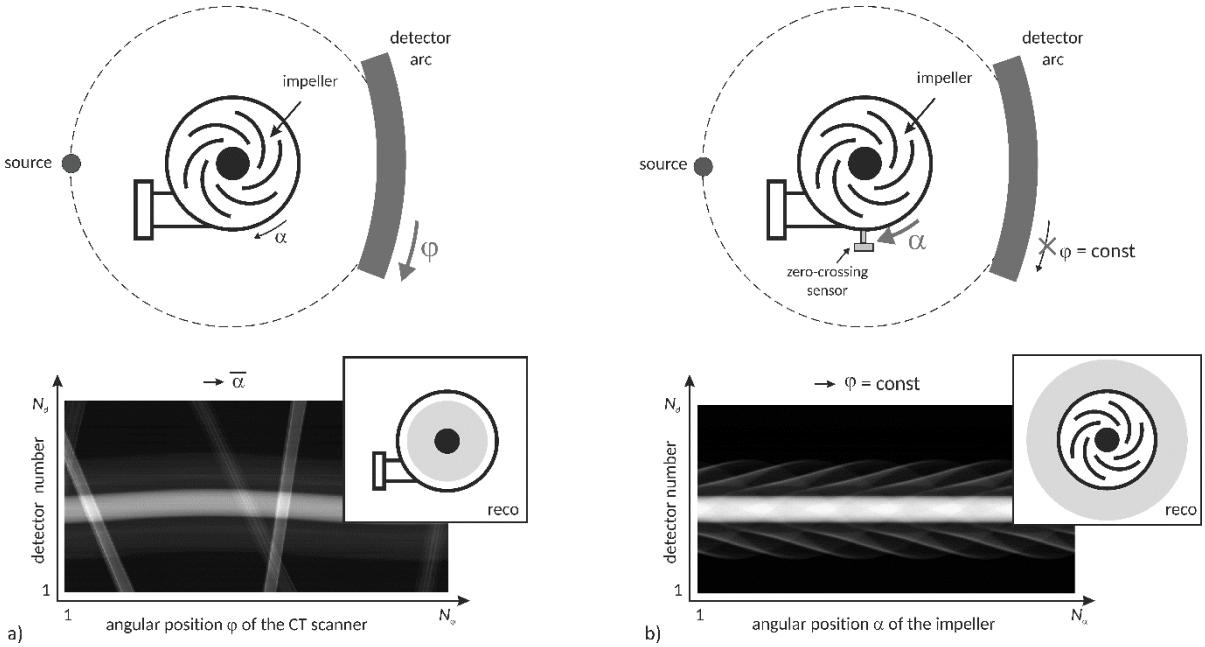

Figure 1: Scheme of setup and imaging procedure (top), obtained sinograms (bottom) and schematic view of reconstructed images (inset) with sharp (black) and angular-averaged (gray) structures exemplarily shown for a centrifugal pump applying a) *conv*CT and b) *tar*CT imaging.

As mentioned above, for *tar*CT imaging projection data have to be acquired for a number of rotations N_r. Thus, a three-dimensional data matrix $S^{\mathrm{tar}}_{d,j,t}$ is initially generated, where the index t is defined as $t \in \mathbb{N} \mid 0 \leq t < N_r$ and the index j is defined as $j = N_\alpha\,\Delta t_j/\Delta t_{zc}$. The interval Δt_j denotes the residual time since the last zero-crossing. By integrating over all revolutions and dividing by the total time $t_{zc} \cdot N_r/N_\alpha$ per projection angle, the count rates

$$\dot{S}^{\mathrm{tar}}_{d,j} = \frac{1}{t_{zc} \cdot N_r/N_\alpha} \cdot \sum_{t=1}^{N_r} S^{\mathrm{tar}}_{d,j,t} \tag{5}$$

are calculated representing radiographic projections of the rotating parts of the pump taken in the rotating frame, i.e. the impeller and all the parts including the liquid holdup rotating at the same speed (see Figure 1b).

For *advCT imaging* both previously described CT imaging methods are simultaneously performed. To obtain the sinogram data for *conv*CT and *tar*CT from one measurement, a three-dimensional data matrix $\dot{S}^{\mathrm{adv}}_{d,i,j}$ of the dimensions $N_d \times N_\varphi \times N_\alpha$ is defined at first (see Figure 2, middle). The source-detector assembly is then rotated around the object. At the first quasi-stationary projection position $i = 1, \varphi_0 = 0°$ a time-averaged angle-resolved data set $\dot{S}^{\mathrm{adv}}_{d,i=1,j} = \dot{S}^{\mathrm{tar}}_{d,j}$ is obtained according to the procedure described above. This is repeated for each subsequent projection angle $\varphi_i = 2\,\pi(i-1)/N_\varphi$. After an entire rotation of the source-detector assembly $\dot{S}^{\mathrm{adv}}_{d,i,j}$ contains N_φ sub-matrices with $i \in \mathbb{N} \mid 0 \leq i < N_\varphi$ each representing a single time-averaged angle-resolved sinogram obtained by varying the projection angle $\varphi_i = 2\,\pi i/N_\varphi$ of the source-detector assembly (see Figure 2, top).

Given the object to be positioned in the very center of the source-detector assembly and provided that $N_\varphi = N_\alpha$, an extended time-averaged angle-resolved sinogram

$$\dot{S}^{\mathrm{tar}}_{d,j} = \frac{1}{N_\varphi} \cdot \sum_{i=1}^{N_\varphi} \dot{S}^{\mathrm{adv}}_{d,i,j^*} \qquad \text{with } j^* = (j-i) \bmod j \tag{6}$$

can simply be obtained by averaging shifted versions of $\dot{S}^{\mathrm{adv}}_{d,i,j}$ containing projections with the best photon statistic. The projection shift $j^* = (j-i) \bmod j$ in $\dot{S}^{\mathrm{adv}}_{d,i,j^*}$ compensates the angular offset between the applied *tar*CT synchronization sensor, e.g. Hall sensor, and the associated projection angle φ_i of the CT imaging system (see Figure 2, bottom, right). Averaging $\dot{S}^{\mathrm{adv}}_{d,i,j}$ over all rotation angles *j*, the conventional sinogram

$$\dot{S}^{\mathrm{conv}}_{d,i} = \frac{1}{N_\alpha} \cdot \sum_{j=1}^{N_\alpha} \dot{S}^{\mathrm{adv}}_{d,i,j} \tag{7}$$

is obtained (see Figure 2, bottom, left).

For each j the sub-matrix $\dot{S}^{\mathrm{adv}}_{d,i,j=\mathrm{const}}$ represents a conventional sinogram for a given (static) impeller angle position (see Figure 3). Eventually, a combined image can be reconstructed showing both the focused stationary structures as well as the rotating structures ‘frozen’ at an angular position $\alpha_j = 2\,\pi j/N_\alpha$. It should be mentioned, that the image is still an ensemble-average obtained over many rotations. Nevertheless, this combined CT imaging approach is practical, if structures in the object change repeatedly with the identical course for every revolution. In case of the centrifugal pump, this holds for fluid elements that enter the pump in the center and move towards the tangential outlet. Thus, such permanently occurring radial flow can be visualized with this CT imaging mode. Therefore,

frozen-impeller images are reconstructed for all impeller angles α. The resulting image sequence shows how ensemble-averaged structures move with the rotating impeller during one revolution.

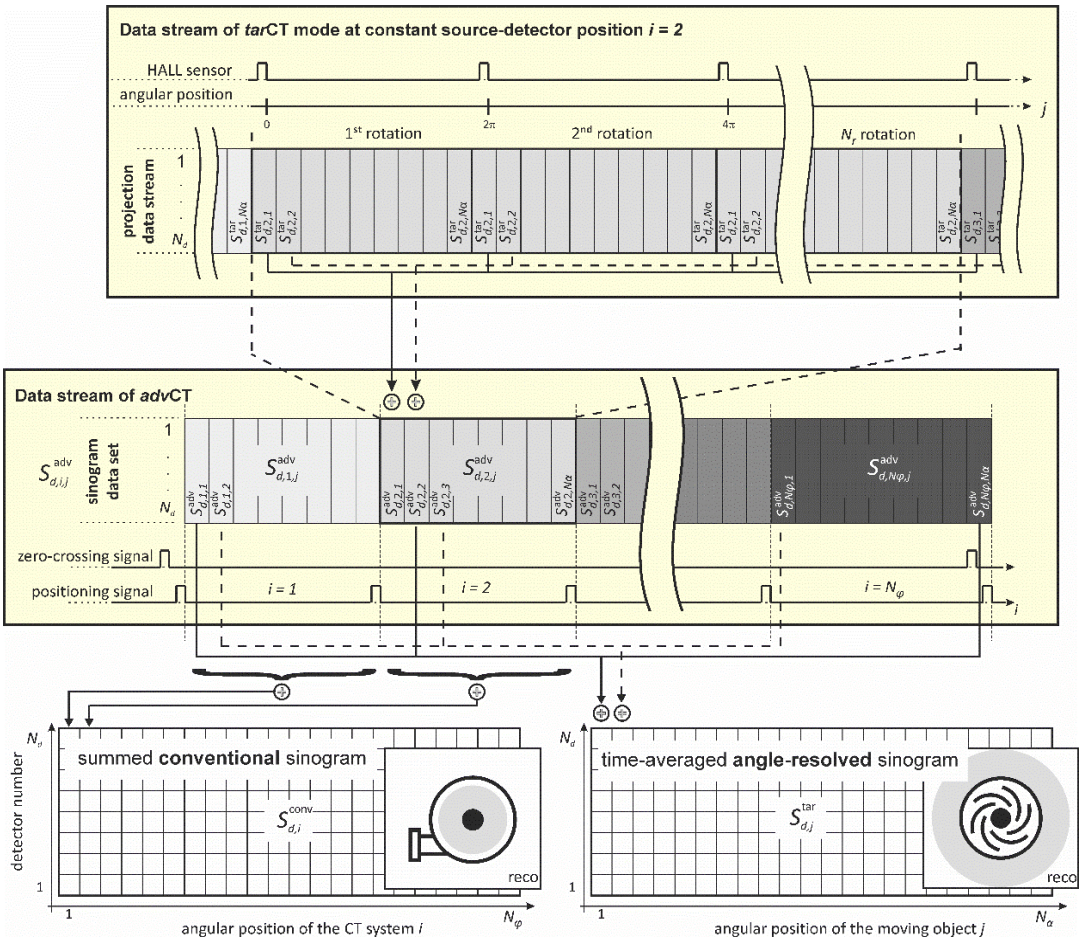

Figure 2: Schematics of the projection data stream analysis to restructure projection data according to both *tar*CT and *conv*CT using a data set provided by the *adv*CT imaging method.

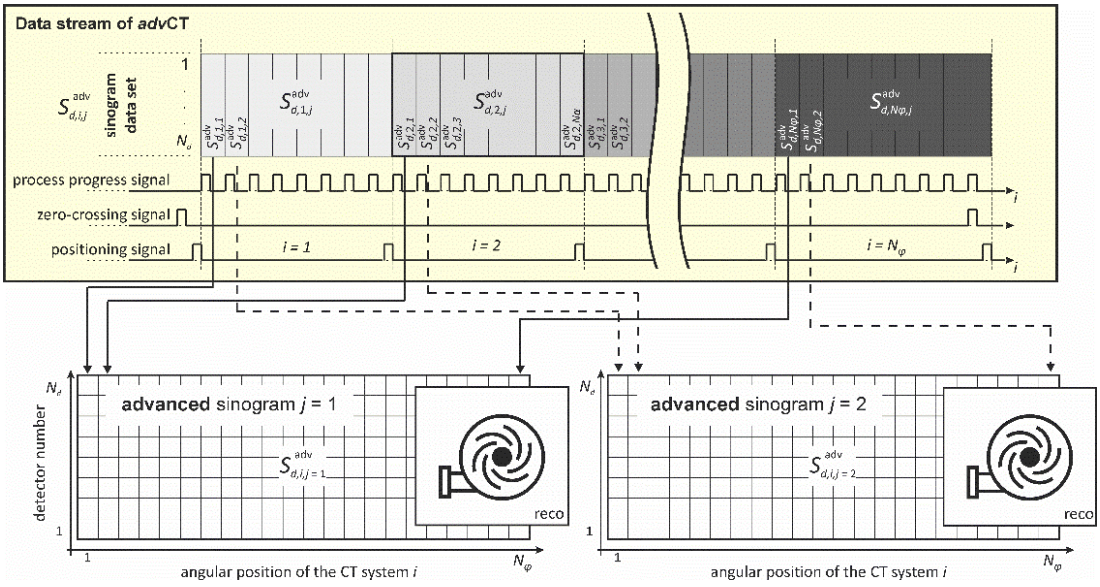

Figure 3: Schematics of the projection data stream analysis to restructure projections according to *adv*CT for two different angular positions of the impeller, which rotates at 1480 rpm.

2.2 Gamma-ray CT scanner

The applied high-resolution gamma-ray CT scanner (HireCT) mainly comprises a collimated ^{137}Cs source with an activity of about 185 GBq and a photon energy of 662 keV as well as a radiation detector arc composed of $N_d = 320$ scintillation detector elements positioned opposite to the source. Each detector pixel has an active area of 2 mm by 4 mm and provides a radiation detection efficiency of about 75% for 662 keV gamma photons. The detector arc is focused to a distance of 970 mm and is operated in single photon count mode, which is very important at low photon fluxes, high projection data sampling frequencies or at a combination of both. Hitherto, the HireCT was operated in either *conv*CT or *tar*CT imaging mode [14], [29].

For *conv*CT imaging, the HireCT is typically rotated slowly between $f^{\mathrm{CT}} = 0.33\ \mathrm{mHz}$ (0.02 rpm) and $f^{\mathrm{CT}} = 1.67\ \mathrm{mHz}$ (0.1 rpm). Accordingly, the data sampling frequency and its corresponding data stream rate is rather low and hence not critical. The projection data acquisition is triggered by two light barrier sensors directly mounted on the rotary stage. The first light barrier indicates the zero-crossings, i.e. angular reference position. The second sensor delivers a crossing signal at every 0.36° interval using a mechanically perforated ring with $N_\varphi = 1000$ equidistantly distributed measuring points.

For *tar*CT imaging, the HireCT is fixed and provides a projection data sampling frequency of up to $f^{\mathrm{samp}} = 22\ \mathrm{kHz}$, which is sufficient to sample rapidly moving parts, such as impellers of axial and centrifugal pumps [33] or fluid couplings [30], [31]. Therefore, an additional very fast data acquisition and transfer electronics is used and an advanced detector value read-out procedure is performed. For process-synchronization, two binary status signals are connected to the electronics and are directly implemented into the projection data stream.

To perform *adv*CT imaging, the positioning information of the HireCT is recorded with the existing fast data acquisition and transfer electronics. Therefore, the electrical signals of both light barrier sensors were initially connected to the existing microprocessor via a dual optoelectronic coupler. Further, the microprocessor firmware was modified to integrate the binary status of both light barrier sensors into the existing status byte, in which already two status signals for the process synchronisation sensors were coded. This way, the modified fast data acquisition electronics is able to sample four external binary signals, while the size of the data stream and the data sampling frequency f^{samp} is retained.

3. Results

The *adv*CT imaging mode and the modified HireCT scanner are applied to an industrial centrifugal pump (Etachrom BC 032-160074 C11, KSB, Germany) with a closed radial multi-vane impeller forming six fluid conveying chambers. The pump was already investigated by Schäfer et al. [34] and Neumann et al. [33] concerning their gas-liquid flow operation behaviour. In this study, a constant volumetric gas fraction of 2.6 % is charged with the conveyed liquid (tap water). The diameter of the impeller is 125 mm, which rotates with a speed of $f^{\mathrm{pump}} = 1480\ \mathrm{rpm}$. An external Hall effect sensor provides the zero-crossing signals for each revolution of the pump impeller corresponding to a time interval of $\Delta t_{zc} = 40.54\ \mathrm{ms}$ per revolution.

Eventually, *adv*CT of the centrifugal pump operated with single-phase liquid and two-phase gas/liquid flow are performed with a total duration of 50 min, i.e. each *tar*CT scan is performed for three seconds. A single projection scan $\dot{S}_d^{\mathrm{ref}}$ without any object and with sufficient photon statistic is used as reference for calculating the absolute radiation attenuation values. Projection data pre- and post-processing are accomplished as described in Chapter 2.2 using GNU Octave v4.2.1. Simultaneous iterative reconstruction technique (SIRT) was performed with 50 iteration steps on a graphic processing unit by the open-source CT reconstruction tool ASTRA v1.8 [37]-[39]. Slice images are reconstructed on a 1440 × 1440 pixel grid with a pixel size of 0.5 mm. For this purpose, the obtained fan beam sinogram is resorted and interpolated to a parallel beam sinogram with virtual 3600 detector elements and 1800 projections for a 180° rotation.

As shown in Figure 4, the results of both standard CT imaging methods (*conv*CT and *tar*CT) could be successfully extracted from the *adv*CT scan using Equations (6) and (7). It can be seen from the *conv*CT sinogram that the driving shaft of the impeller is not exactly positioned in the very centre of the HireCT system. Thus, in addition to Equation (6), each *tar*CT sinogram $\dot{S}^{\mathrm{adv}}_{d,i=\mathrm{const},j}$ is slightly shifted along the detector axis to achieve an overlap of the driving shaft in the final averaged *tar*CT sinogram $\dot{S}^{\mathrm{tar}}_{d,j^*}$. The empirically identified shifting sinus curve from the *conv*CT will reduce the optimal spatial resolution of the *tar*CT scan to a negligible degree.

Prior to reconstructing the image sequence from the *adv*CT, the following additional artificial process synchronisation is performed. As the impeller consists of six identical constructed and rotation-symmetrically arranged chambers, each sixth part of the sinogram $\dot{S}^{\mathrm{adv}}_{d,i,j}$ is averaged with respect to *j* (see Figure 5) in order to significantly improve the photon statistic. Nevertheless, possible pulsations

of the gas phase towards the tangential outlet of the centrifugal pump are still visible in the averaged *adv*CT sinogram stack $\dot{S}^{\mathrm{adv}}_{d,i,j^{\#}}$ with $N_\alpha = N_\alpha/6$. In Figure 6, five exemplarily reconstructed cross-sectional images are shown in which the impeller is visualised in different angular positions ranging from 0° to 48° with increments of 12° (note that the 60° position coincides with the 0° position).

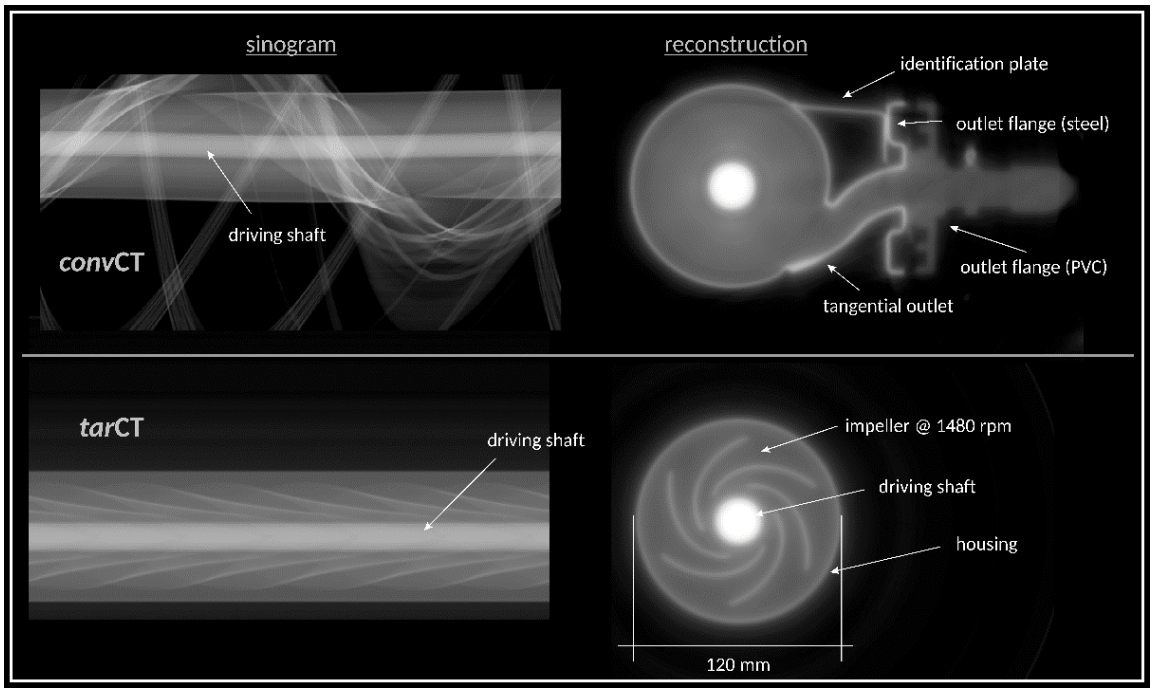

Figure 4: Comparison of *conv*CT imaging (top) and *tar*CT imaging (bottom) using the improved electronics of the HireCT for the centrifugal pump (impeller is rotating with 1480 rpm) that enables *adv*CT imaging.

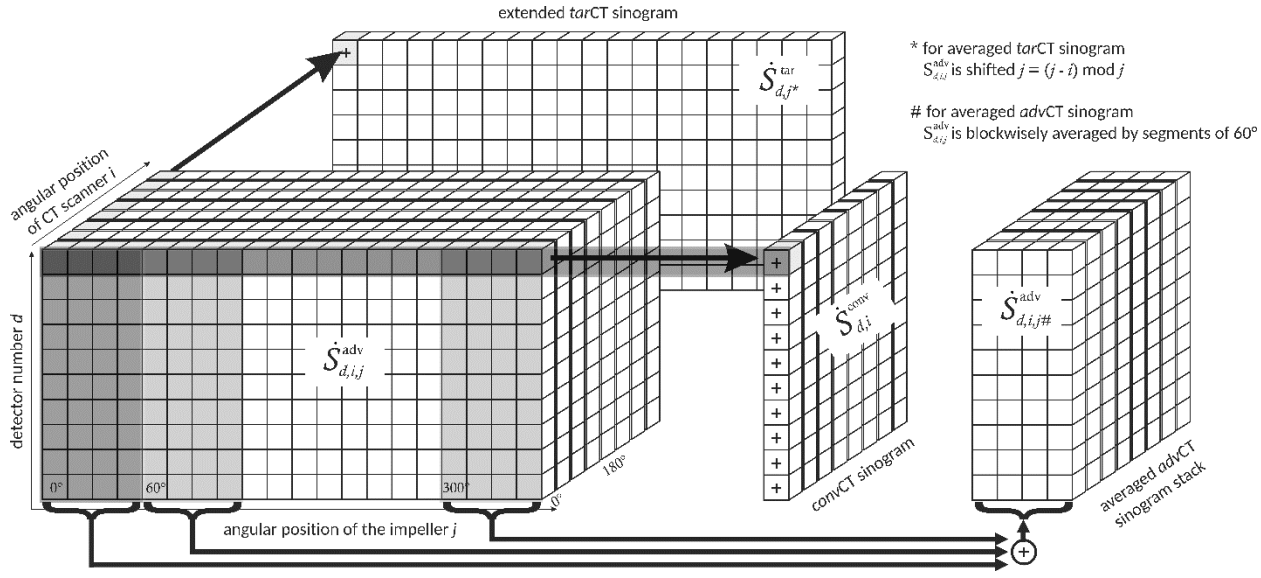

Figure 5: Illustration of the data sorting procedure of the *adv*CT data stack to extract *conv*CT and *tar*CT sinograms and an averaged *adv*CT sinogram stack as well.

For the calculation of the gas fraction distributions, reconstructed absolute images of the centrifugal pump operated at two-phase flow conditions are subtracted with the images obtained from the centrifugal pump operated at single-phase liquid flow conditions and subsequently normed to the attenuation value of the liquid phase. The results are compiled in Figure 7. For a better orientation, an absolute reconstruction of the centrifugal pump is shown in the top left position.

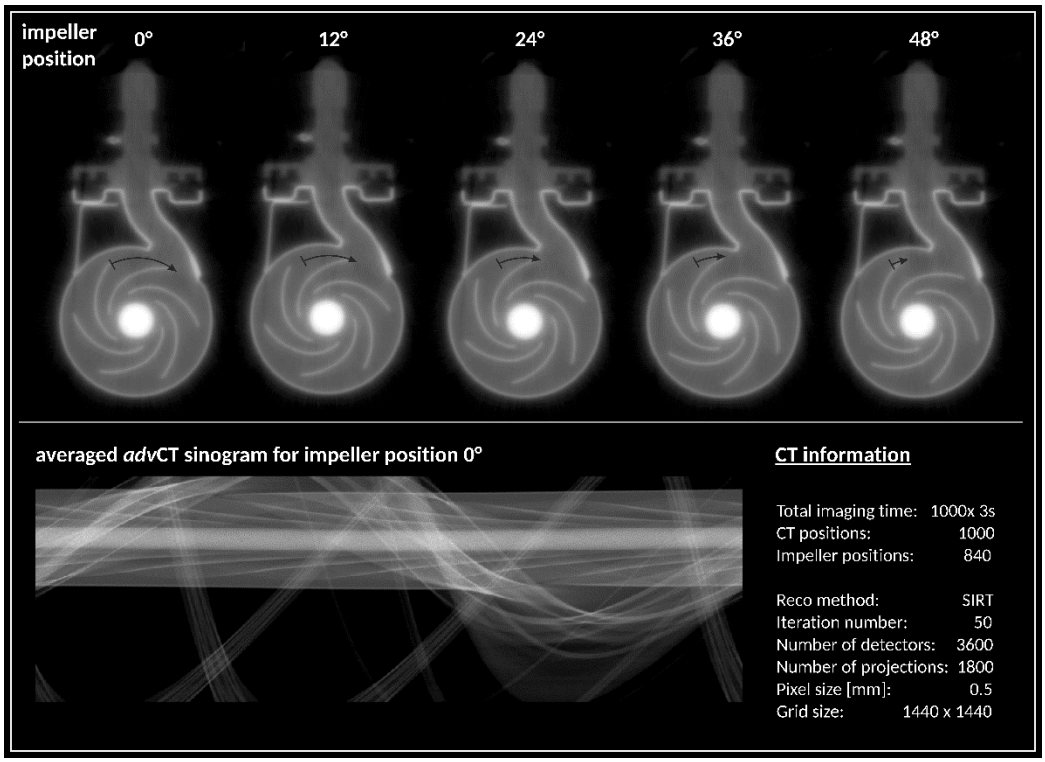

Figure 6: Reconstructions of the centrifugal pump at five different angular positons of its impeller operated at 1480 rpm.

From the averaged *conv*CT imaging (Figure 7, top, centre) an asymmetric gas pocket is identified near the tangential outlet of the centrifugal pump (highlighted by the red circle), representing continuously ejected gas fraction. Furthermore, *conv*CT imaging reveals a gas dead zone directly behind the tangential outlet. In contrast, the result from averaged *tar*CT imaging (Figure 7, top, right) shows no asymmetric gas phase distribution with respect to the impeller geometry. However, it can be recognized that the gas phase is homogeneously distributed in all six chambers and the gas fraction is significantly higher compared to the injected volumetric gas fraction of 2.6 %. Thus, it can be concluded that a static or dynamic gas pocket is generated within the impeller region that impedes the transport of the liquid (see also [33], [34]).

Eventually, the image sequence obtained by the averaged *adv*CT imaging procedure is visualized for selected angular positions of the impeller (Figure 7, bottom). Again gas-rich and gas-lean zones can be identified. In contrast to the averaged *tar*CT, both scenarios can now be studied in its dynamics, i.e. depending on the angular position of the impeller.

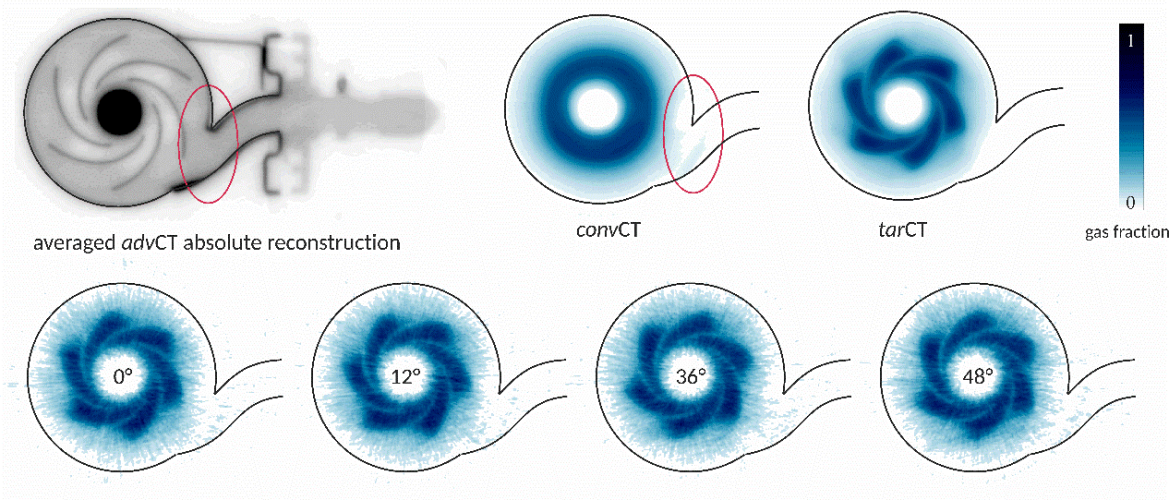

Figure 7: Visualization of the gas fraction distribution in a centrifugal pump (top, left) operated in gas-liquid two-phase flow applying *adv*CT imaging using the HireCT imaging system. Results of the *conv*CT (top, centre), the *tar*CT (top, right) and results of the averaged *adv*CT (bottom line) are shown. (Colours available in the online version)

4. Conclusion

In this paper, an advanced process-synchronized computed tomography (*adv*CT) imaging approach was presented that combines the pros of two standard CT imaging methods, namely conventional CT (*conv*CT) and time-averaged angle-resolved CT (*tar*CT). After presenting their basic principles, the *adv*CT imaging was introduced from which data of both standard CT imaging methods can be extracted. Additionally, using a new data sorting procedure, cross-sectional image sequences at different process progress stages with sharp structures of both the static and the synchronized dynamic parts were obtained. The novel *adv*CT was exemplarily proved on a centrifugal pump whose impeller rotated with 1480 rpm. Eventually, quantitative phase fraction distributions were calculated and investigated. Various static and dynamic flow processes could be clearly revealed. Thus, the amount of information was significantly increased using the novel *adv*CT imaging.

5. References

[1] C. Kak, M. Slaney, Principles of Computerized Tomographic Imaging, *IEEE Press*, New York, (1988).

[2] R. Gordon, R. Bender, G. T. HERMAN, Algebraic Reconstruction Techniques (ART) for three-dimensional Electron Microscopy and X-ray Photography, *J. Theor. Biol*. 29, 471-481, (1970).

[3] Willi A. Kalender, Computed Tomography: Fundamentals, System Technology, Image Quality, Applications, 3rd Edition (2011), ISBN: 978-3-895-78317-3

[4] Wang Y, Vidan E, Bergman GW. Cardiac motion of coronary arteries: variability in the rest period and implications for coronary MR angiography. Radiology 213, 751–758, (1999).

[5] Flohr T, Kuttner A, Bruder H, et al. Performance evaluation of a multi-slice CT system with 16-slice detector and increased gantry rotation speed for isotropic submillimeter imaging of the heart. Herz 28, 7–19, (2003).

[6] Flohr T, Stierstorfer K, Raupach R, Ulzheimer S, Bruder H. Performance evaluation of a 64-slice CT system with z-flying focal spot. Rofo 176, 1803–1810, (2004).

[7] W.A. Kalender, W. Seissler, E. Klotz, P. Vock. Spiral volumetric CT with single-breathhold technique, continuous transport, and continuous scanner rotation. Radiology, 176/1, 181-183, (1990).

[8] M. Kachelrieß, S. Ulzheimer, W.A. Kalender. ECG-correlated imaging of the heart with subsecond multi-slice spiral CT. IEEE Transactions on Medical Imaging 19/9, 888-901, (2000).

[9] H. Seifarth, S. Wienbeck, M. Püsken, K.-U. Juergens, D. Maintz, Ch. Vahlhaus, W. Heindel, R. Fischbach, Optimal Systolic and Diastolic Reconstruction Windows for Coronary CT Angiography Using Dual-Source CT, American Journal of Roentgenology 189, 1317-1323, (2007). https://doi.org/10.2214/AJR.07.2711

[10] B. Lu, S.S. Mao, N. Zhuang, H. Bakhsheshi, H. Yamamoto, J. Takasu, S. Liu, M. J. Budoff, Coronary Artery Motion During the Cardiac Cycle and Optimal ECG Triggering for Coronary Artery Imaging, Investigative Radiology 36/5, 250-256, (2001).

[11] O. Lindgren, J. Davis, P. Wells, P. Shadbolt, Non-destructive wood density distribution measurements using computed tomography, Holz als Roh-und Werkstoff 50, 295, (1992). https://doi.org/10.1007/BF02615356

[12] I. Amenabar, A. Mendikute, A. López-Arraiza, M. Lizaranzu, J. Aurrekoetxea, Comparison and analysis of non-destructive testing techniques suitable for delamination inspection in wind turbine blades, Composites Part B: Engineering 42/5, 1298-1305, (2011). https://doi.org/10.1016/j.compositesb.2011.01.025

[13] D. J. Bull, L. Helfen, I. Sinclair, S. M. Spearing, T. Baumbach, A comparison of multi-scale 3D X-ray tomographic inspection techniques for assessing carbon fibre composite impact damage, Composites Science and Technology 75, 55-61, (2013). https://doi.org/10.1016/j.compscitech.2012.12.006

[14] U. Hampel, A. Bieberle, D. Hoppe, J. Kronenberg, E. Schleicher, T. Suehnel, W. Zimmermann, C. Zippe, High resolution gamma ray tomography scanner for flow measurement and non-destructive testing applications, *Review of Scientific Instruments* 78, 103704, (2007).

[15] A. Kemoun, B. C. Ong, P. Gupta, M. Al-Dahhan, M. P. Dudukovic, Gas holdup in bubble columns at elevated pressure via computed tomography, *International Journal of Multiphase Flow* 27, 929-946, (2007).

[16] U.P. Veera, Gamma ray tomography design for the measurement of hold-up profiles in two-phase bubble columns, *Chemical Engineering Journal* 81, 251–260, (2001).

[17] A. Bieberle, H. Nehring, R. Berger, M. Arlit, H.-U. Härting, M. Schubert, U. Hampel, Compact high-resolution gamma-ray computed tomography system for multiphase flow studies, Rev. Sci. Instrum. 84, 033106, (2013).

[18] G. A. Johansen, T Frøystein, B. T. Hjertaker, Ø Olsen, A dual sensor flow imaging tomographic system, Meas. Sci. Technol. 7, 297–307, (1996).

[19] Kok, H.V., Hagen, T.H.J.J., Mudde, R.F., Subchannel void-fraction measurements in a 6×6 rod bundle using a simple gamma-transmission method, International Journal of Multiphase Flow 27, 147–170, (2001).

[20] R. Rollbusch et al., Experimental investigation of the influence of column scale, gas density and liquid properties on gas holdup in bubble columns, International Journal of Multiphase Flow 75, 88-106, (2015). https://doi.org/10.1016/j.ijmultiphaseflow.2015.05.009

[21] A. Bieberle et al., Gamma-ray computed tomography for imaging of multiphase flows, Chemie Ingenieur Technik Vol. 85 / 7, 1002-1011, (2013). https://doi.org/10.1002/cite.201200250

340 [22] H.-U. Haerting et al., Hydrodynamics of co-current two-phase flow in an inclined rotating tubular
341 fixed bed reactor – Wetting intermittency via periodic catalyst immersion, Chemical Engineering
342 Science 128, 147-158, (2015).
343 https://doi.org/10.1016/j.ces.2015.02.008
344 [23] M. A. Leon et al., Hydrodynamics and Gas-Liquid Mass Transfer in a Horizontal Rotating Foam
345 Stirrer Reactor, Chemical Engineering Journal 217/1, 10-21, (2012).
346 https://doi.org/10.1016/j.cej.2012.11.104
347 [24] R. Tschentscher et al., Gas holdup of rotating foam reactors measured by γ-tomography - effect
348 of solid foam pore size and liquid viscosity, AIChE Journal 59(1), 146-154, (2013).
349 https://doi.org/10.1002/aic.13787
350 [25] R. Tschentscher et al., Tomography measurements of gas-holdup in rotating foam reactors with
351 Newtonian, non-Newtonian and foaming liquids, Chemical Engineering Science, 66/14, 3317-
352 3327, (2011).
353 https://doi.org/10.1016/j.ces.2011.01.051
354 [26] M. Schubert, G. Hessel, C. Zippe, R. Lange, U. Hampel, Liquid flow texture analysis in trickle bed
355 reactors using high-resolution gamma ray tomography, *Chemical Engineering Journal* 140/(1-3),
356 332-340, (2008).
357 [27] F. Vischer et al., Water and n-heptane volume fractions in a rotor-stator spinning disc reactor,
358 Industrial & Engineering Chemistry Research 51, 16670-16676, (2012).
359 https://doi.org/10.1021/ie301439s
360 [28] H.-M. Prasser, D. Baldauf, J. Fietz, U. Hampel, D. Hoppe, C. Zippe, J. Zschau, M. Christen, G. Will,
361 Time resolving gamma-tomography for periodically changing gas fraction fields and its
362 application to an axial pump, *Flow Measurement and Instrumentation* 14, 119–125, (2003).
363 [29] A. Bieberle, E. Schleicher, U. Hampel, Data acquisition system for angle synchronized gamma-ray
364 tomography of rapidly rotating objects, *Measurement Science and Technology* 18, 3384-339,
365 (2007).
366 [30] U. Hampel, D. Hoppe, K.-H. Diele, J. Fietz, H. Höller, R. Kernchen, H.-M. Prasser, C. Zippe,
367 Application of gamma tomography to the measurement of fluid distributions in a hydrodynamic
368 coupling, *Flow Measurement and Instrumentation* 16, 85–90, (2005).
369 [31] A. Bieberle et al., Hydrodynamics analysis in micro-channels of a viscous coupling using gamma-
370 ray computed tomography, Flow Measurement and Instrumentation 45, 288-297, (2015).
371 https://doi.org/10.1016/j.flowmeasinst.2015.07.008

372 [32] H.-M. Prasser et al., Time Resolving Gamma-Tomography for Periodically Changing Gas Fraction
373 Fields, Flow Measurement and Instrumentation 14, 119-125, (2003).
374 https://doi.org/10.1016/S0955-5986(03)00010-4
375 [33] M. Neumann et al., An experimental study on the gas entrainment in horizontally and vertically
376 installed centrifugal pumps, Journal of Fluids Engineering 138 (09130), 1-9, (2016).
377 https://doi.org/10.1115/1.4033029
378 [34] T. Schaefer et al., Application of gamma-ray computed tomography for the analysis of gas
379 holdup distributions in centrifugal pumps, Flow Measurement and Instrumentation 46, 262-267,
380 (2015).
381 https://doi.org/10.1016/j.flowmeasinst.2015.06.001
382 [35] M. Haghnegahdar, S. Boden, U. Hampel, Investigation of mass transfer in milli-channels using
383 high-resolution microfocus X-ray imaging, International Journal of Heat and Mass Transfer 93,
384 653-664, (2016).
385 https://doi.org/10.1016/j.ijheatmasstransfer.2015.10.033
386 [36] A. Landelle, N. Tauveron, R. Revellin, P. Haberschill, S. Colasson, V. Roussel, Performance
387 investigation of reciprocating pump running with organic fluid for organic Rankine cycle, Applied
388 Thermal Engineering 113, 962-969, (2017).
389 http://dx.doi.org/10.1016/j.applthermaleng.2016.11.096
390 [37] W. van Aarle, W. J. Palenstijn, J. Cant, E. Janssens, F. Bleichrodt, A. Dabravolski, J. De
391 Beenhouwer, K. J. Batenburg, and J. Sijbers, “Fast and Flexible X-ray Tomography Using the
392 ASTRA Toolbox”, *Optics Express*, 24(22), 25129-25147, (2016).
393 http://dx.doi.org/10.1364/OE.24.025129
394 [38] W. van Aarle, W. J. Palenstijn, J. De Beenhouwer, T. Altantzis, S. Bals, K. J. Batenburg, and J.
395 Sijbers, “The ASTRA Toolbox: A platform for advanced algorithm development in electron
396 tomography”, *Ultramicroscopy*, 157, 35–47, (2015).
397 http://dx.doi.org/10.1016/j.ultramic.2015.05.002
398 [39] W. J. Palenstijn, K. J. Batenburg, and J. Sijbers, “Performance improvements for iterative
399 electron tomography reconstruction using graphics processing units (GPUs)”, *Journal of*
400 *Structural Biology*, vol. 176/2, 250-253, (2011).
401 http://dx.doi.org/10.1016/j.jsb.2011.07.017